Reducing Hysteresis and Enhancing Performance of Perovskite Solar Cells Using Low-Temperature Processed Y-Doped SnO_2 Nanosheets as Electron Selective Layers

Guang Yang, Hongwei Lei, Hong Tao, Xiaolu Zheng, Junjie Ma, Qin Liu, Weijun Ke, Zhiliang Chen, Liangbin Xiong, Pingli Qin, Zhao Chen, Minchao Qin, Xinhui Lu, Yanfa Yan, and Guojia Fang**

***D**espite the rapid increase of efficiency, perovskite solar cells (PSCs) still face some challenges, one of which is the current–voltage hysteresis. Herein, it is reported that yttrium-doped tin dioxide (Y-SnO_2) electron selective layer (ESL) synthesized by an in situ hydrothermal growth process at 95 °C can significantly reduce the hysteresis and improve the performance of PSCs. Comparison studies reveal two main effects of Y doping of SnO_2 ESLs: (1) it promotes the formation of well-aligned and more homogeneous distribution of SnO_2 nanosheet arrays (NSAs), which allows better perovskite infiltration, better contacts of perovskite with SnO_2 nanosheets, and improves electron transfer from perovskite to ESL; (2) it enlarges the band gap and upshifts the band energy levels, resulting in better energy level alignment with perovskite and reduced charge recombination at NSA/perovskite interfaces. As a result, PSCs using Y-SnO_2 NSA ESLs exhibit much less hysteresis and better performance compared with the cells using pristine SnO_2 NSA ESLs. The champion cell using Y-SnO_2 NSA ESL achieves a photovoltaic conversion efficiency of 17.29% (16.97%) when measured under reverse (forward) voltage scanning and a steady-state efficiency of 16.25%. The results suggest that low-temperature hydrothermal-synthesized Y-SnO_2 NSA is a promising ESL for fabricating efficient and hysteresis-less PSC.*

1. Introduction

In recent years, organic–inorganic perovskite solar cells (PSCs) have gained extensive attention due to their excellent properties in photovoltaic application. The power conversion efficiency (PCE) of lead halide PSCs has rapidly increased from an initial 3.8% to 22.1% during the past several years.[1–9] Such an excellent performance of PSC is greatly attributed to

G. Yang, H. Lei, Dr. H. Tao, X. Zheng, J. Ma, Q. Liu,
Dr. W. Ke, Z. Chen, Dr. L. Xiong, Dr. P. Qin, Z. Chen, M. Qin,
Prof. G. J. Fang
Key Lab of Artificial Micro- and Nano-Structures of
Ministry of Education of China
School of Physics and Technology
Wuhan University
Wuhan 430072, P. R. China
E-mail: gjfang@whu.edu.cn

DOI: 10.1002/smll.201601769

Dr. W. Ke, Prof. Y. F. Yan
Department of Physics and Astronomy
and Wright Center for Photovoltaics Innovation
and Commercialization
The University of Toledo
Toledo, OH 43606, USA
E-mail: yanfa.yan@utoledo.edu
M. Qin, Dr. X. Lu
Department of Physics
The Chinese University of Hong Kong
New Territories, Hong Kong 999077, P. R. China

© 2016 Wiley-VCH Verlag GmbH & Co. KGaA, Weinheim

some distinct properties of perovskite materials, including high absorption coefficient and very long carrier lifetime.[4,5,10,11] Despite the rapid increase of record cell efficiency, PSCs still face some challenges such as Pb toxicity, degradation, and current–voltage (*J*–*V*) hysteresis. The *J*–*V* hysteretic effects of perovskite solar cells have been intensively studied. So far, various origins have been reported for the hysteretic effects, including charge-trapping at interfaces and grain boundaries and capacitive, ion migration, and ferroelectric effects.[12–16] Fortunately, effective approaches, such as using mesoporous electron selective layers (ESLs) or fullerene interface passivation, have been found to be able to reduce or even eliminate the hysteresis of perovskite solar cells.[17–20] The state-of-the-art cells use thin mesoporous TiO_2 ESLs.[21,22] However, effective TiO_2 ESLs usually require high temperature processing, which is disadvantageous for commercialization of PSCs. Low-temperature processed metal oxide ESLs are preferred for the fabrication of low-cost PSCs. So far, effective ZnO, SnO_2, and WO_x ETLs can be synthesized by low-temperature processes,[23–27] and most efficient PSCs using these low-temperature processed ESLs have the planar cell configuration. Without fullerene passivation, these cells inevitably exhibit a high degree of hysteresis in the *J*–*V* measurements, largely due to the inefficient electron transfer at the metal oxide/perovskite interfaces.[28–30] Using mesoporous metal oxide, ESL can increase ESL/perovskite contact regions and therefore improve charge transfer at the interfaces, leading to the capacitive charges quickly dissipated by charge separation.[16] Aside from mesoporous nanoparticles, 1D TiO_2 nanorods,[31,32] nanofibers,[33] nanocones,[34] and ZnO nanorods,[35,36] have been used to facilitate electron transfer at ESL/perovskite interfaces.[37] 2D SnO_2 nanosheets have been proven to exhibit good light-collection efficiency and fast electron transport abilities in dye-sensitized solar cells.[38,39] However, to the best of our knowledge, using well-aligned 2D SnO_2 nanosheet arrays (NSAs) as ESL has never been reported in PSCs.

It has been reported that doping can be an effective way to improve the properties of ESLs and ESL/perovskite interfaces. For example, incorporating some aliovalent cations, such as Nb^{5+}, Al^{3+}, Mg^{2+}, and Y^{3+} in TiO_2 can obviously improve the carrier transport abilities and optical and electrical properties of TiO_2, leading to enhanced efficiencies of perovskite solar cells.[40–43] Doping could also improve the electrical and optical properties of ZnO by manipulating the morphology, which has been successfully employed in the ZnO-based PSCs.[23,36]

In this work, for the first time, we demonstrate low-temperature in situ hydrothermal-synthesized yttrium-doped SnO_2 (Y-SnO_2) NSAs for significantly reducing the hysteresis and enhancing the performance of PSCs. We show that Y doping can effectively promote the formation of well-aligned and homogeneously distributed Y-SnO_2 NSAs, ensuring a high infiltration of perovskite and improved electron transfer, leading to PSCs with very low *J*–*V* hysteresis. Besides, Y-doped SnO_2 shows enhanced conductivity, ensuring facilitated charge extraction and transport. Y doping is also found to optimize the energy level matching between ESL and perovskite, resulting in improved cell efficiencies. The champion cell using Y-SnO_2 NSA ESL achieves a photovoltaic conversion efficiency of 17.21% (17.05%) when measured under reverse (forward) voltage scanning and a steady-state PCE of 16.25%. Our results suggest that low-temperature hydrothermal synthesized Y-SnO_2 NSA is a promising ESL for fabricating efficient perovskite solar cells with low hysteresis.

2. Results and Discussion

2.1. Device Structure

Figure 1a shows the schematic of our perovskite solar cell configuration. The low-temperature processed Y-SnO_2 layer was directly deposited on a fluorine-doped SnO_2 (FTO) substrate via one-step in situ hydrothermal synthesis. The Y-SnO_2 layer was composed of a compact Y-SnO_2 layer and a mesostructured SnO_2 nanosheet layer and it served as the ESL. The $CH_3NH_3PbI_3$ absorber was deposited by one-step spin-coating of a perovskite precursor and annealing at 100 °C for 15 min. The 2,2′,7,7′-tetrakis-(*N*,*N*-di-pmethoxyphenylamine)-9,9′-spirobifluorene (spiro-OMeTAD) hole transport layer (HTL) was spin coated on the top of the perovskite layer and then the Au electrode was deposited by thermal evaporation. The cross-sectional image of a Y-SnO_2-based mesostructured PSC device is shown in Figure 1b. The energy band diagram of our device is depicted in Figure 1c.

2.2. Crystal Structure and Morphologies of SnO_2 and Y-SnO_2 NSAs

The X-ray diffraction (XRD) patterns of SnO_2 thin films prepared by a hydrothermal process are presented in Figure S1a (Supporting Information). The XRD curves of SnO_2 and Y-SnO_2 nanosheets show four diffraction peaks (110), (101), (200), and (211) at 2θ = 27°, 34°, 38°, and 52°. No phase related to Y was found for the Y-SnO_2 thin film. The diffraction peak positions of Y-SnO_2 films tended to shift toward higher angles and peaks become slightly broader, indicating that the Y^{3+} ions should be partly incorporated into the SnO_2 without disruption of the crystalline structure. The crystallite size of SnO_2 was caculated using the Debye–Scherrer formula ($D = 0.89 \cdot \lambda / \beta \cdot \cos\theta$), where λ is the X-ray wavelength, θ is the Bragg diffraction angle, and β is the peak width at half maximum. The values for the average size of crystallites are similar for both SnO_2 and Y-SnO_2 samples. To exclude the impact of FTO substrates, we have performed grazing incidence wide angle X-ray scattering (GIWAXS) of thin film samples deposited on FTO glass substrates, shown in Figure S1b (Supporting Information). The diffraction peak can be observed when the incident angle (θ = 0.2°) is small enough, representing the structure information of the SnO_2 films grown on the FTO substrate, as this avoids overlap with a diffuse scattering background from the substrate. When the incident angle increases (θ = 1.5°), the structure information of FTO substrates becomes prominent. This result demonstrates the crystalline nature of hydrothermal-synthesized SnO_2 nanosheets.

© 2016 Wiley-VCH Verlag GmbH & Co. KGaA, Weinheim

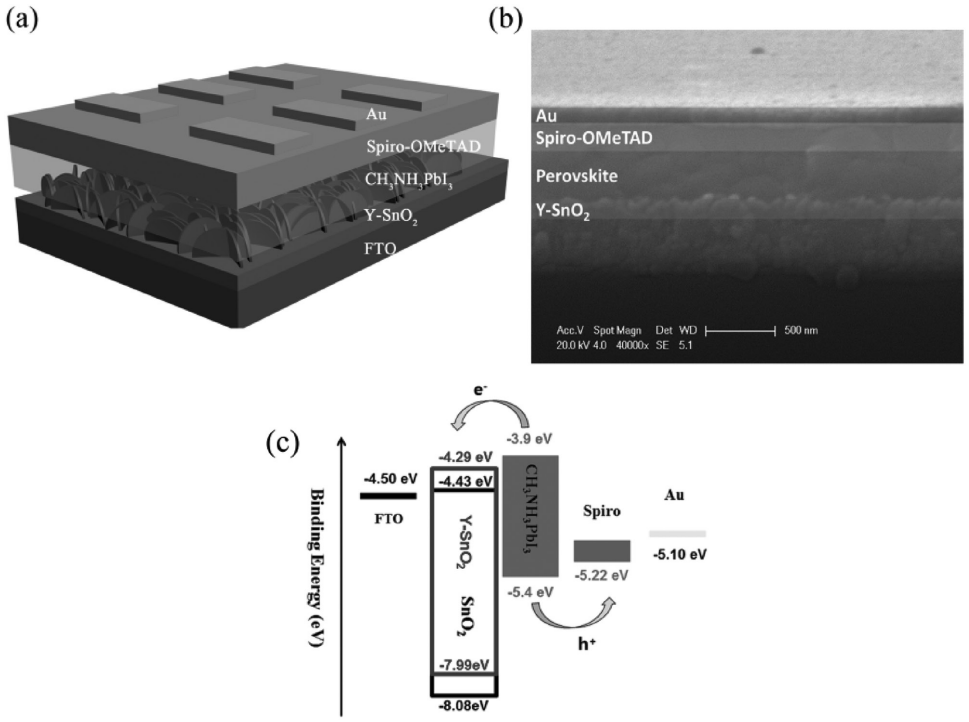

Figure 1. a) Schematic view and b) the color-enhanced cross-sectional SEM image of a completed perovskite solar cell using a Y-SnO_2 ESL. c) Energy band diagram of our perovskite solar cell.

The X-ray photoelectron spectroscopy (XPS) measurements were performed to investigate the chemical composition of the SnO_2 and Y-SnO_2 thin film samples and the results are depicted in Figure S2 (Supporting Information). The binding energies of 487.11 and 495.56 eV correspond to the Sn $3d_{5/2}$ and $3d_{3/2}$ peaks (Figure S2a,b, Supporting Information), respectively, which are observed from both SnO_2 and Y-SnO_2 samples. The core level spectrum of Y 3d was solely observed from the Y-SnO_2 sample. Figure S2c (Supporting Information) shows the XPS results of Y 3d states describing Y 3d peak at 158.58 eV, which was attributed to the $3d_{3/2}$ states of Y^{3+}.[45,46] It indicates that Y substitutes Sn in the lattice of SnO_2 as the oxide state of Y^{3+}. The results derived from XPS reveal that the Y is successfully incorporated into SnO_2 samples.

We find that Y doping can promote the formation of well-aligned and homogeneously distributed SnO_2 NSAs. **Figure 2**a shows schematically the hydrothermal growth of SnO_2 and Y-SnO_2 nanosheets on FTO glass. The whole hydrothermal reaction does not need high temperature and high pressure conditions and could be suitable for large area applications. The resultant SnO_2 and Y-SnO_2 thin films could be used to fabricate perovskite solar cells without annealing. Figure 2b–e shows the scanning electron microscope (SEM) images of the surfaces of SnO_2 and Y-SnO_2 thin films deposited on FTO substrates at different magnifications. It is clearly seen that the Y-SnO_2 thin film consists of many well-aligned nanosheets (Figure 2d). However, the SnO_2 nanosheets are not homogeneously distributed in the pure SnO_2 sample. Leaf-like nanosheets are clearly visible in the Y-SnO_2 sample. As shown in Figure S3 (Supporting Information), Y-SnO_2 nanosheets became thicker and larger when the Y additive concentration was increased. However, the heavily Y-doped SnO_2 NS is not a good candidate as ESL for efficient PSC, possibly due to too much recombination occurring at the Y-SnO_2 ESL/perovskite interface. To verify the charge transfer and charge recombination at the ESL/perovskite interface, the electrochemical impedance spectroscopy analysis was performed at 0.8 V in the dark. Figure S4 (Supporting Information) presents the Nyquist plots of PSCs based on SnO_2 with different Y doping content. It has been reported that the first (in the high frequence range) and second semicircles (in the low frequency range) were assigned to charge transfer resistance (R_{tr}) and charge recombination resistance (R_{rec}) at the ESL/perovskite interface, respectively.[46] When the doping amount of Y is 3%, the lowest R_{tr} and the highest R_{rec} were observed, implying the enhanced injection and transfer of electrons and the reduced charge recombination. We found that 3% Y-doped SnO_2 could produce perovskite solar cells with the best performance. However, the perovskite solar cells with 5% and 20% Y-doped SnO_2 has a higher R_{tr} and lower R_{rec}, which are not suitable for efficient selective contact layers. Therefore, Y-SnO_2 refers to 3% Y-doped SnO_2 in the following section. The hydrothermal reaction solution becomes more acidic with the increase of hydrolysis of Y^{3+}. Research has shown that SnO_2 is easily formed under acidic conditions, which is beneficial to the formation of highly ordered Y-SnO_2 films.[47] Moreover, from the cyclic voltammetry (CV) measurements shown in Figure S5 (Supporting Information), the hydrothermal-synthesized SnO_2 and Y-SnO_2 films can completely block the charge transfer from FTO to the electrolyte, which indicates these films are pin-hole free. A slight difference in voltammogram for SnO_2 and Y-SnO_2 can be ascribed

 © 2016 Wiley-VCH Verlag GmbH & Co. KGaA, Weinheim

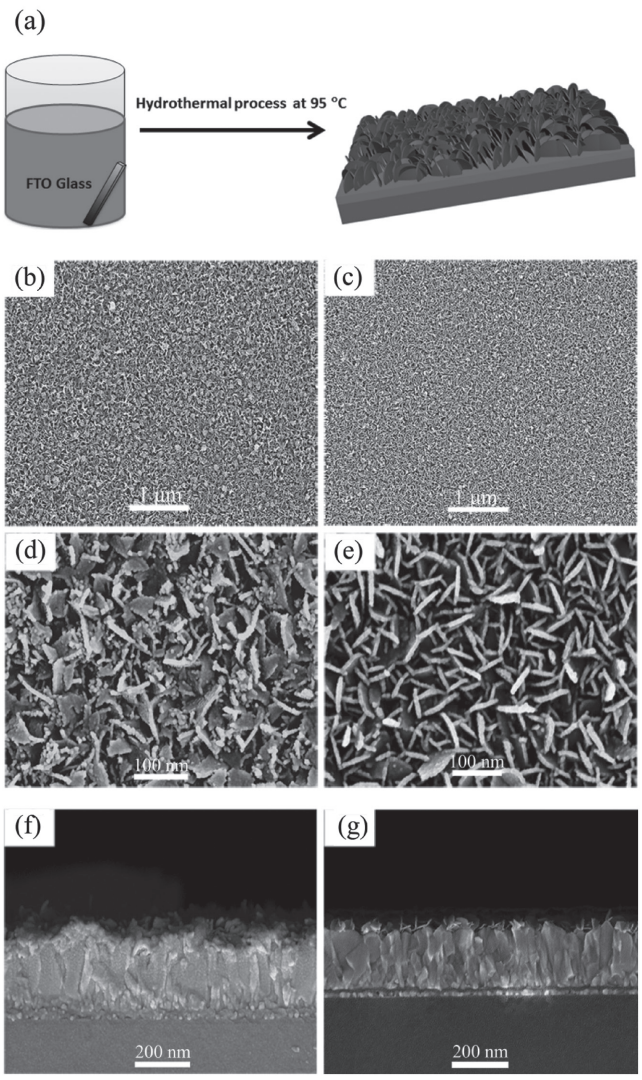

Figure 2. a) Sketch of the low-temperature in situ hydrothermal process to fabricate SnO_2 and Y-SnO_2 nanosheet thin films on FTO. Top view SEM images of a SnO_2 film at b) low and d) high magnifications, and a Y-SnO_2 film at c) low and e) high magnifications and cross-sectional SEM images of f) a SnO_2 film and g) a Y-SnO_2 film.

to the change of conductivity after Y-doping of SnO_2, which will be discussed in the following section. **Figure 3**f,g shows the cross-sectional SEM image of the nanostructured SnO_2 and Y-SnO_2 films. The nanosheets with rectangular cross-section are uniformly distributed on the FTO substrate in the Y-SnO_2 sample.

2.3. Photovoltaic Performance of PSCs

The photovoltaic performance of the PSCs with SnO_2 and Y-SnO_2 ESLs were investigated under simulated one-sun illumination (AM 1.5G). Figure 3c shows the *J*–*V* characteristics of PSCs with different ESLs. The device based on Y-SnO_2 ESLs achieved a PCE of 17.29% (16.97%) with open circuit voltage (V_{OC}) of 1.08 (1.08) V, short circuit current density (J_{SC}) of 22.55 (22.45) mA cm^{-2}, and fill factor (FF) of 71% (70%) when measured under reverse voltage scanning. For comparison, the cell with the SnO_2-ESL device showed a PCE of 13.38% (10.15%) with a V_{OC} of 1.05 (1.03) V, a J_{SC} of 19.31 (19.32) mA cm^{-2}, and FF of 66% (51%) when measured under reverse (forward) voltage scanning. **Table 1** summarizes the average J_{SC}, V_{OC}, FF, and PCE values of the corresponding 40 devices. As we can see from the data, it is notable that the device using Y-SnO_2 ESL performs much better than the device using SnO_2 ESL. The enhancement in cell efficiency mainly came from the improvement in the J_{SC} from 19.31 to 22.55 mA cm^{-2}, V_{OC} from 1.05 to 1.08 V, and FF from 66% to 71%. The FF of Y-SnO_2-based device exhibits an obviously higher value than that of SnO_2, resulting from improved interfacial connection between SnO_2 and perovskite after Y-doping, decreasing sheet resistance. It has been demonstrated that the film morphology of the perovskite absorber layer can affect device performance. The SEM surface images of the perovskite layer depositing on SnO_2 and Y-SnO_2 ESL are shown in Figure S6 (Supporting Information). No significant morphological difference of perovskite layers, such as surface coverage, crystallinity, and grain size was found in these two types of samples. Cross-sectional views of perovskite films deposited on the SnO_2 and Y-SnO_2 ESLs are shown in Figure S7 (Supporting Information). It illustrates that Y-SnO_2 film has better interfacial contact with the perovskite layer. Hence, device performance enhancement by employing Y-SnO_2 ESL is likely attributed to better energy alignment, enhanced contact properties, and the improvement of carrier transfer at ESL/perovskite interface.

Figure S8 (Supporting Information) shows the plots of $-dV/dJ$ versus $(J_{SC}–J)^{-1}$ and linear fitting curves of perovskite solar cells using different ESLs (SnO_2 and Y-SnO_2) under illumination. The ideality factor (A), series resistance (R_s), and shunt resistance (R_{sh}) of solar cells are derived from the slope and intercept of the linear fitting results. The R_s of the SnO_2-based and Y-SnO_2-based devices are 7.11 and 4.07 Ω cm^2, respectively. The R_{sh} of the SnO_2-based and Y-SnO_2-based devices are 800 and 2500 Ω cm^2, respectively. The corresponding results are summarized in **Table 2**. The device using Y-SnO_2 ESL shows a relatively lower R_s and higher R_{sh} compared to the SnO_2 based device, which may be one reason for different device photovoltaic performance. Reduced lower R_s and higher R_{sh} are beneficial for achieving higher J_{SC}, V_{OC}, and FF, which probably results from the increased interface area between Y-SnO_2 NSAs and the perovskite layer.[48] Moreover, the ideality factor (A) is a little decreased, which indicates suppression in charge recombination.[49]

To further understand the differences in photocurrent densities between devices using SnO_2 and Y-SnO_2 ESLs, optical transmittance spectra of SnO_2 and Y-SnO_2 films were measured and shown in Figure 3a. It is interesting to note that low-temperature hydrothermal processed SnO_2 and Y-SnO_2 films can both improve the optical transmission properties of FTO substrates, resulting from good antireflection ability of SnO_2 thin film.[25] Since the refractive indices are different for different wavelengths of the light, the effect of the reflectance reduction depends on the wavelength; thus, the difference of the refractive indices between the FTO substrates and SnO_2 antiflection films would influence reflectance and optical absorption.[50] We think homogeneously distributed Y-SnO_2

 © 2016 Wiley-VCH Verlag GmbH & Co. KGaA, Weinheim

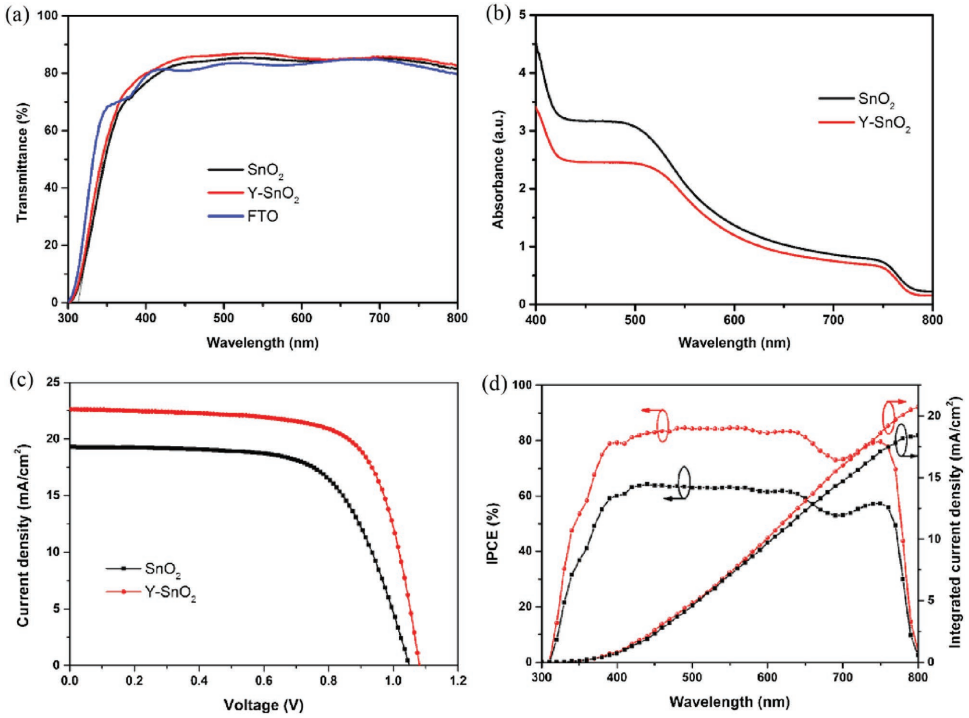

Figure 3. a) Transmittance spectra of FTO substrates with SnO_2 and Y-SnO_2 ESLs. b) UV–vis absorbance spectra of perovskite solar films grown on SnO_2 and Y-SnO_2 ESLs. c) *J–V* curves of the perovskite solar cells using SnO_2 and Y-SnO_2 ESLs under reverse voltage scanning. d) IPCE spectra of the cells using SnO_2 and Y-SnO_2 ESLs.

nanosheets can reduce light scattering and increase the transmittance of light. The growth of SnO_2 nanosheets on FTO substrates is a benefit from the homoepitaxial substrates. The Y-SnO_2 film on FTO shows better optical transmittance properties than SnO_2 film, which allows more photoflux to reach the absorber layer for photogenerated carriers. This is possibly because homogeneous Y-SnO_2 film shows better morphology than SnO_2 film. The light-harvesting efficiency of the PSCs using SnO_2 and Y-SnO_2 ESLs are also investigated by using the absorption spectrum. Figure 3b presents the ultraviolet–visible absorption spectra of the perovskite films with the same thickness deposited on the SnO_2 and Y-SnO_2 films. It is obvious that the absorption of the perovskite film over almost the entire visible spectrum is enhanced on Y-SnO_2 film than that on SnO_2 film. This result can be attributed to the increased interfacial contact and a higher loading of perovskite material on the highly ordered porous framework of mesostructured Y-SnO_2 film compared with SnO_2 film.[51,52] This improved optical absorption properties of perovskite film deposited on Y-SnO_2 nanosheets may enable the perovskite absorber layer to harvest more light, and hence a higher J_{SC} can be obtained for device using Y-SnO_2 ESL. In addition to the improved optical properties and interfacial contacts, Y-SnO_2 also showed the enhanced conductivity compared with the SnO_2. The current–voltage (*I–V*) curves of SnO_2 and Y-SnO_2 films in the structure of Au/SnO_2 (or Y-SnO_2)/Au were measured using a semiconductor parameter analyzer (4200-SCS, Keithley, USA), shown in Figure S9 (Supporting Information).[53] The conductivity of SnO_2 and Y-SnO_2 was estimated to be from 7.5×10^{-6} to 1.05×10^{-5} S cm^{-1}, respectively. The enhanced conductivity can lower the contact resistance and facilitate the charge extraction, benefitting the improved J_{SC}. Figure 3d shows the measured incident photon-to-current conversion efficiency (IPCE) spectra of the cells using SnO_2 ESL and Y-SnO_2 ESL. The device-based Y-SnO_2 exhibits higher IPCE than the device-based SnO_2 over the entire wavelength range, indicating a superior charge injection and collection of the Y-SnO_2 ESL. The integrated current densities based on these curves are 18.4 and 20.9 mA cm^{-2} for the cells using the SnO_2 ESL and Y-SnO_2 ESL, respectively, which are slightly lower than the J_{SC} obtained from the corresponding *J–V* measurements.

We noted that the V_{OC} of the Y-SnO_2-based device (1.08 V) is higher than that of SnO_2-based device (1.05 V), which probably stems from two causes. On one hand, the aligned Y-SnO_2 NSAs provide effective charge extraction and

Table 1. Average photovoltaic parameters of the perovskite solar cells with SnO_2 and Y-SnO_2 ESLs for 40 separated devices.

ESLs	V_{OC} [V]	J_{SC} [mA cm^{-2}]	FF	PCE_{ave} [%]
SnO_2	1.03 ± 0.02	18.62 ± 0.31	0.61 ± 0.14	11.69 ± 0.40
Y-SnO_2	1.07 ± 0.01	21.80 ± 0.25	0.67 ± 0.11	15.60 ± 0.35

Table 2. Photovoltaic performance of perovskite solar cells employing SnO_2 and Y-SnO_2 ESLs with the highest PCE.

ESLs	V_{OC} [V]	J_{SC} [mA cm^{-2}]	FF [%]	PCE [%]	R_s [Ω cm^2]	R_{sh} [Ω cm^2]	A
SnO_2	1.05	19.31	66	13.38	7.11	800	2.96
Y-SnO_2	1.08	22.55	71	17.29	4.07	2500	2.58

© 2016 Wiley-VCH Verlag GmbH & Co. KGaA, Weinheim

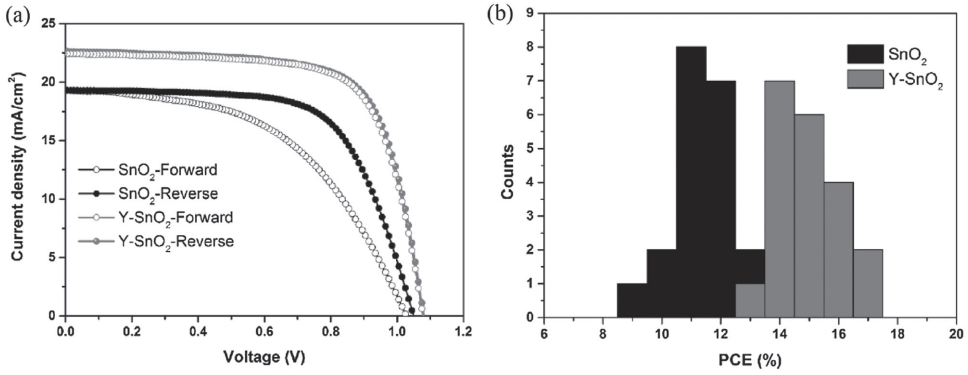

Figure 4. a) *J–V* curves of the perovskite solar cells using SnO_2 and Y-SnO_2 ESLs under reverse and forward voltage scanning. b) Histograms of PCEs for 20 cells with SnO_2 ESLs and 20 cells with Y-SnO_2 ESLs measured under reverse voltage scanning.

transport properties.[54] On the other hand, Y-SnO_2 exhibits a better energy level alignment with perovskite layer, resulting in a higher V_{OC} of perovskite solar cells.[55,56] Our previous work has shown that doping TiO_2 with Mg^{2+} can shift its conduction band (CB) upward and decrease the recombination, and thus increase the V_{OC} output.[42] Hence, we confirmed the change of energy levels of the two different ESLs by ultraviolet photoelectron spectroscopy (UPS) and transmission spectra measurement (Figure S10, Supporting Information). First, we calculated the band gap of SnO_2 and Y-SnO_2 by plotting the diagram of $(\alpha h\upsilon)^2$ against $h\upsilon$ obtained from the transmission spectra in Figure S10a (Supporting Information). It clearly shows that SnO_2 film exhibits a slightly wider band gap after Y-doping; the band gaps of the SnO_2 film and Y-SnO_2 film are 3.65 and 3.70 eV, respectively. The Fermi levels (E_F) of SnO_2 and Y-SnO_2 obtained from UPS are 5.19 and 5.11 eV (Figure S10b, Supporting Information), respectively. $E_F - E_V$ of both SnO_2 and Y-SnO_2 are 2.88 eV (Figure S10c, Supporting Information). Therefore, the calculated conduction band minimum (CBM) of Y-SnO_2 is ≈0.13 eV higher than that of SnO_2. The value of $|E_{CBM} - E_F|$ for the Y-SnO_2 is larger than that of SnO_2. Thus, compared with SnO_2, a lower concentration of electrons in the CB of the Y-SnO_2 can induce reduced interface combination. Besides, a higher conduction band minimum level of SnO_2 is also desired for higher V_{OC}. Hence, the devices using Y-SnO_2 ESL have higher V_{OC} than those using SnO_2 ESL.

The anomalous photocurrent hysteresis was always observed in many PSCs, which maybe originated from several causes, such as ion migration and charge accumulation at interface, and so on.[14,17,57,58] The contact interface has a big effect on the transient process in PSCs, which may give rise to hysteresis behavior of the device. The electrical contact interface between perovskite and ESL can be a significant factor influencing the hysteresis behavior of the device.[29] We found that PSCs using Y-SnO_2 ESL showed less *J–V* hysteresis than that using SnO_2 ESL. It is believed that the porous network provided by Y-SnO_2 NSAs exhibit improved interfacial contact and excellent charge transport abilities, which contributes to reducing *J–V* hysteresis of PSCs.[36] The photogenerated electron can effectively extract and transport across the interface between ESLs and perovskite layer after Y doping, and thus *J–V* hysteresis is reduced, as demonstrated in other reports.[59–61] The *J–V* curves of devices employing Y-SnO_2 ESL and SnO_2 ESL with respect to scan direction are both shown in **Figure 4**a. The solar cell based on Y-SnO_2 ESL showed a PCE of 17.29% (16.97%) with a V_{OC} of 1.08 (1.08) V, a J_{SC} of 22.45 (22.55) mA cm^{-2}, and a FF of 71% (70%) when measured under the reverse (forward) voltage scanning. The solar cell with SnO_2-ESL device showed a PCE of 13.38% (10.15%) with a V_{OC} of 1.05 (1.03) V, a J_{SC} of 19.31 (19.32) mA cm^{-2}, and FF of 66% (51%) when measured under reverse (forward) voltage scanning. The photovoltaic performances of best-performing perovskite solar cells using SnO_2 and Y-SnO_2 ESLs with respect to different scanning directions are summarized in **Table 3**. Besides, the *J–V* curves measured under different voltage scanning rates are shown in Figure S11 (Supporting Information), revealing a negligible difference in *J–V* curves obtained from different scanning rates for Y-SnO_2 ESL-based PSC.

To illustrate the effect of Y-doping of SnO_2 on device hysteretic behavior, we have made a comparative study on the charge extraction and electron transport behavior of devices with SnO_2 and Y-SnO_2 ESLs. The carrier extraction behavior of different ESLs was studied by the steady state photoluminescence (PL) quenching experiment and time-resolved photoluminescence (TRPL). As presented in **Figure 5**a, more efficient PL quenching is observed with the perovskite film grown on the Y-SnO_2 film than the film grown on SnO_2 film. This PL quenching is due to charge carrier extraction enhancement across the interface between ESL and perovskite layer. Y doping of SnO_2 results in an increase in PL quenching, indicating efficient electron transport and charge extraction at the Y-SnO_2 ESL/perovskite interface. As

Table 3. Summary of best-performing device parameters obtained in different scanning directions for pristine SnO_2 and Y-SnO_2, under one sun illumination (AM 1.5G, 100 mW cm^{-2}).

Sample	Scan direction	V_{OC} [V]	J_{SC} [mA cm^{-2}]	FF [%]	PCE [%]
Pristine SnO_2	Reverse	1.05	19.31	66	13.38
	Forward	1.03	19.32	51	10.15
Y-SnO_2	Reverse	1.08	22.55	71	17.29
	Forward	1.08	22.45	70	16.97

© 2016 Wiley-VCH Verlag GmbH & Co. KGaA, Weinheim

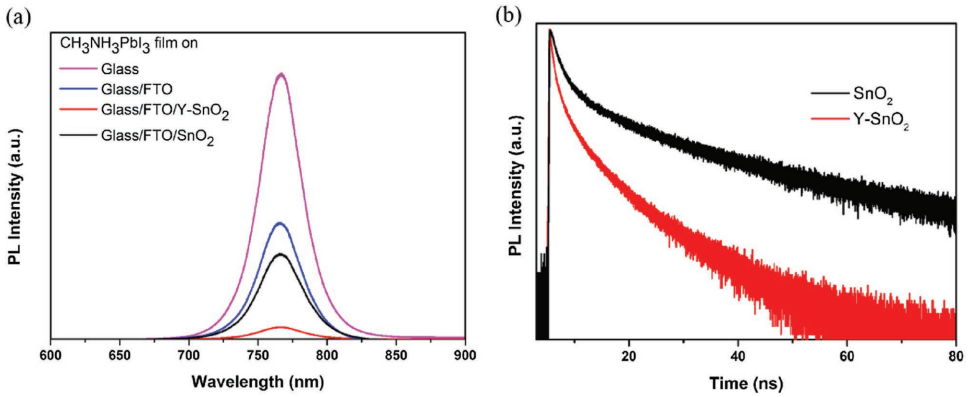

Figure 5. a) PL spectra of perovskite films: Glass/$CH_3NH_3PbI_3$ (pink line), Glass/FTO/$CH_3NH_3PbI_3$ (blue line), Glass/FTO/SnO_2/$CH_3NH_3PbI_3$ (black line), Glass/FTO/Y-SnO_2/$CH_3NH_3PbI_3$ (red line). b) TRPL spectra of $CH_3NH_3PbI_3$ films grown on SnO_2 (black line) and Y-SnO_2 (red line) coated substrates.

expected, the improved interfacial contact and enhanced conductivity mentioned above can contribute to the improved injection and transfer of electrons and reduced charge accumulation. This enhancement can prevent the accumulation of excess capacitive charge that leads to hysteresis.[19,62] The charge transport behavior of SnO_2 and Y-SnO_2 ESLs was further investigated by the TRPL spectra (Figure 5b). The TRPL decay curves were exponentially fitted. For the SnO_2/$CH_3NH_3PbI_3$ sample, $\tau 1$ is 20.333 ns (67.22%) and $\tau 2$ is 1.744 ns (32.78%), resulting in an amplitude average lifetime of 14.239 ns. For the Y-SnO_2/$CH_3NH_3PbI_3$ sample, $\tau 1$ is 6.384 ns (53.5%) and $\tau 2$ is 0.547 ns (46.5%), with an amplitude average lifetime of 2.381 ns. Therefore, it is apparent that the photon-induced electrons transfer from perovskite to Y-SnO_2 ESL is faster and more effective than that from perovskite to SnO_2 ESL. The improvement of charge extraction and transport ability would decrease charge accumulation at the interface, leading to reduced *J*–*V* hysteresis.

To check the effect of Y-doping of SnO_2 ESL on the device performance, we measured 40 different solar cells under the same conditions. The efficiency distribution of the devices is shown in Figure 4b and is summarized in Table 1. The average efficiency of Y-SnO_2-based devices (15.6%) is much higher than that of SnO_2 (11.05%), and Y-SnO_2-based devices show a narrow distribution of PCEs than the SnO_2-based devices. These results indicate that the reproductivity of devices is significantly enhanced after Y doping.

The steady-state power output at a given constant forward bias near the maximum output power point of the solar cell is another important parameter to evaluate the real PCE of perovskite devices with hysteresis. Therefore, we measured the steady-state efficiencies of the best-performing cells using SnO_2 and Y-SnO_2 ESLs and the corresponding results are shown in **Figure 6**. The solar cell using a Y-SnO_2 ESL achieved a steady-state current density of 18.90 mA cm^{-2} and a steady-state efficiency of 16.25% at a constant bias voltage of 0.86 V, which is very close to the value averaged from the efficiencies measured under forward and reverse voltage scanning, whereas the solar cell using SnO_2 ESL achieved a steady-state current density of 15.27 mA cm^{-2} and a steady-state efficiency of 12.23% at a constant bias voltage of 0.80 V. In addition, we also fabricated the cells with large active area (1 cm^2) employing the hydrothermal-synthesized homogeneous Y-SnO_2 ESL. Figure S12 (Supporting Information) shows the *J*–*V* curve of the best-performing device with an active area of 1 cm^2. It shows a PCE of 12.60% and the detail of photovoltaic performance is presented in the inset of Figure S12 (Supporting Information).

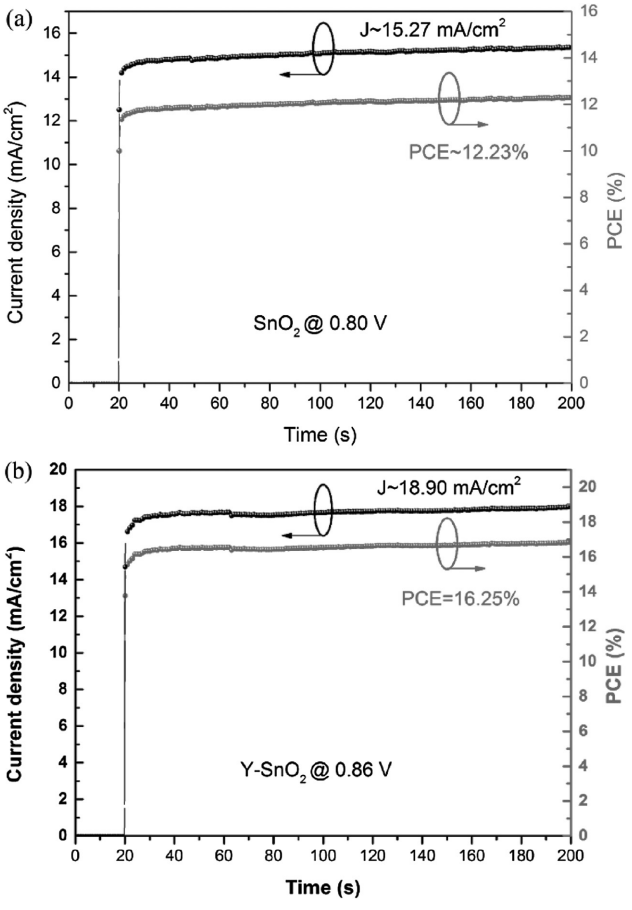

Figure 6. Steady-state efficiencies of perovskite solar cells using a) SnO_2 and b) Y-SnO_2 ESLs measured at constant bias voltages of 0.80 and 0.86 V, respectively.

© 2016 Wiley-VCH Verlag GmbH & Co. KGaA, Weinheim

3. Conclusions

In summary, we have studied the effect of Y doping on the morphological, electrical, and optical properties of a SnO_2 nanosheet layer and the performance of perovskite solar cells using Y-SnO_2 ESL. We found that Y-doped SnO_2 NSAs exhibit more positive CBM than undoped SnO_2. Furthermore, Y-doping can promote the formation of well-aligned SnO_2 NSAs, leading to improved perovskite infiltration and enhanced physical, electrical contact with perovskite at the Y-SnO_2 ESL/perovskite interface. As a result, perovskite solar cells using Y-SnO_2 ESL exhibited significantly improved performance with much reduced hysteresis. The champion cell using Y-SnO_2 NSA ESL achieved an efficiency of 17.29% (16.97%) when measured under reverse (forward) voltage scanning and a stabilized power output of 16.25%. Our results suggest that low-temperature processed Y-doped SnO_2 NSAs could be good ESL candidates for producing efficient perovskite solar cells with low hysteresis.

4. Experimental Section

Growth of SnO_2 and Y-SnO_2 Nanosheets: FTO glass substrates (Asahi Glass, 14 Ω sq^{-1}) were cleaned with acetone, ethyl alcohol, and deionized (DI) water several times for proper cleaning. SnO_2 and Y-SnO_2 nanosheets were fabricated by a hydrothermal growth method. The solution was prepared by dissolving equimolar (0.025 M) tin oxalate powder ($Sn(C_2O_4)$, M = 206.73 g mol^{-1}, Aladdin) and hexamethylenetetramine (HMTA, $C_6H_{12}N_4$, M = 140.19 g mol^{-1}, Aladdin, 99.0%) in 50 mL DI water. For Y-SnO_2 nanosheet growth, $Sn(C_2O_4)$, yttrium(III) nitrate hexahydrate ($Y(NO_3)_3 \bullet 6H_2O$), and HMTA were added in 50 mL DI water at a concentration of 0.025 M (molar ratio: 100:3:100). Then, the mixture was stirred under ambient conditions for 1 h. The hydrothermal growth was conducted inside a laboratory oven at 95 °C for 9 h. The obtained SnO_2 and Y-SnO_2 films were rinsed with DI water several times and dried for future use.

Fabrication of Perovskite Solar Cells: First, the SnO_2 and Y-SnO_2 coated FTO substrates were treated with UV-ozone for 15 min before the perovskite film deposition. Next, the perovskite films were deposited through a solvent engineering method. Perovskite precursor solution containing PbI_2 (1 M) and methylammonium iodide (MAI) (1 M) in anhydrous dimethyl formamide (DMF):dimethyl sulfoxide (DMSO) (4:1, volume ratio) was then spin-coated at 1000 rpm for 10 s and then at 4000 rpm for 30 s. During the second step, 500 µL anhydrous diethyl ether was dropped onto the spinning substrates at the first 10 s. The substrates were then annealed at 100 °C for 15 min. The whole process was operated in a nitrogen-filled glovebox. The HTL was prepared by spin-coating the spiro-OMeTAD solution at 3000 rpm for 30 s. The spiro-OMeTAD solution consisted of 73.2 mg spiro-OMeTAD, 28.8 µL 4-tert-butylpyridine (t-BP), 17.5 µL bis(trifluoromethane) sulfonimide lithium salt (Li-TFSi) solution (520 mg in acetonitrile), and 1 mL chlorobenzene. Finally, a ≈80 nm Au layer was deposited via thermal evaporation.

Characterizations: The crystal structures were examined by XRD (Bruker AXS, D8 Advance) with Cu Kα radiation under operation conditions of 40 kV and 40 mA. The morphology of the SnO_2 and Y-SnO_2 films, the whole devices, and the perovskite films were characterized by a high-resolution field emission SEM (JSM 6700F). The GIWAXS measurements were conducted at 23A small- and wide-angle X-ray scattering (SWAXS) beamline at the National Synchrotron Radiation Research Center, Hsinchu, Taiwan, using a 10 keV primary beam, 0.2 and 1.5 incident angle, and C92728DK area detector.[63] The absorption and transmission spectra of the ESLs grown on FTO were measured by an UV–vis spectrophotometer (CARY5000, Varian) in a wavelength range at 300–800 nm at room temperature. XPS and UPS were performed using a XPS/UPS system (Thermo Scientific, ESCLAB 250Xi, USA). PL spectra were obtained with a 532 nm laser, as the excitation source, pulsed at a frequency of 9.743 MHz. The CV experiments were measured in an electrochemical cell with aqueous solution of $Fe(CN)_6^{3-/4-}$ as electrolyte. All the electrochemical measurements were carried out with an electrochemical workstation (CHI 660E, Chenhua, Shanghai). The *J–V* characteristics of the solar cells were measured by a CHI660D electrochemical workstation (Shanghai, China) under a 100 mW cm^{-2} (AM 1.5 simulated irradiation) illumination with a standard ABET Sun 2000 Solar Simulator. The active area was 0.09 cm^2, which was defined by a shadow mask. The hysteresis of the *J–V* curves was recorded at a scan rate of 0.1 V s^{-1}. The external quantum efficiency spectra were measured in air by a QE-R 3011 system (Enli) in the range of 300–800 nm wavelength.

Supporting Information

Supporting Information is available from the Wiley Online Library or from the author.

Acknowledgements

This work was financially supported by the National High Technology Research and Development Program (No. 2015AA050601), the National Natural Science Foundation of China (Nos. 11674252, 61376013, 91433203), the Natural Science Foundation of Jiangsu Province (BK20131186), and the Suzhou Science and Technology Bureau (SYG201449).

[1] H. Zhou, Q. Chen, G. Li, S. Luo, T. B. Song, H. S. Duan, Z. Hong, J. You, Y. Liu, Y. Yang, *Science* **2014**, *345*, 542.
[2] M. Liu, M. B. Johnston, H. J. Snaith, *Nature* **2013**, *501*, 395.
[3] J. Burschka, N. Pellet, S. J. Moon, R. Humphry-Baker, P. Gao, M. K. Nazeeruddin, M. Gratzel, *Nature* **2013**, *499*, 316.
[4] S. D. Stranks, G. E. Eperon, G. Grancini, C. Menelaou, M. J. Alcocer, T. Leijtens, L. M. Herz, A. Petrozza, H. J. Snaith, *Science* **2013**, *342*, 341.
[5] M. M. Lee, J. Teuscher, T. Miyasaka, T. N. Murakami, H. J. Snaith, *Science* **2012**, *338*, 643.
[6] H. S. Kim, C. R. Lee, J. H. Im, K. B. Lee, T. Moehl, A. Marchioro, S. J. Moon, R. Humphry-Baker, J. H. Yum, J. E. Moser, M. Gratzel, N. G. Park, *Sci. Rep.* **2012**, *2*, 591.
[7] J. H. Im, C. R. Lee, J. W. Lee, S. W. Park, N. G. Park, *Nanoscale* **2011**, *3*, 4088.
[8] A. Kojima, K. Teshima, Y. Shirai, T. Miyasaka, *J. Am. Chem. Soc.* **2009**, *131*, 6050.

 © 2016 Wiley-VCH Verlag GmbH & Co. KGaA, Weinheim

[9] W. S. Yang, J. H. Noh, N. J. Jeon, Y. C. Kim, S. Ryu, J. Seo, S. I. Seok, *Science* **2015**, *348*, 1234.
[10] W. J. Yin, T. Shi, Y. Yan, *Adv. Mater.* **2014**, *26*, 4653.
[11] J. M. Frost, K. T. Butler, F. Brivio, C. H. Hendon, M. van Schilfgaarde, A. Walsh, *Nano Lett.* **2014**, *14*, 2584.
[12] W. Tress, N. Marinova, T. Moehl, S. M. Zakeeruddin, M. K. Nazeeruddin, M. Grätzel, *Energy Environ. Sci.* **2015**, *8*, 995.
[13] J. M. Azpiroz, E. Mosconi, J. Bisquert, F. De Angelis, *Energy Environ. Sci.* **2015**, *8*, 2118.
[14] B. Chen, M. Yang, S. Priya, K. Zhu, *J. Phys. Chem. Lett.* **2016**, *7*, 905.
[15] C. Li, S. Tscheuschner, F. Paulus, P. E. Hopkinson, J. Kiessling, A. Kohler, Y. Vaynzof, S. Huettner, *Adv. Mater.* **2016**, *28*, 2446.
[16] H.-S. Kim, N.-G. Park, *J. Phys. Chem. Lett.* **2014**, *5*, 2927.
[17] Y. Shao, Z. Xiao, C. Bi, Y. Yuan, J. Huang, *Nat. Commun.* **2014**, *5*, 5784.
[18] J. Xu, A. Buin, A. H. Ip, W. Li, O. Voznyy, R. Comin, M. Yuan, S. Jeon, Z. Ning, J. J. McDowell, P. Kanjanaboos, J. P. Sun, X. Lan, L. N. Quan, D. H. Kim, I. G. Hill, P. Maksymovych, E. H. Sargent, *Nat. Commun.* **2015**, *6*, 7081.
[19] J. H. Heo, M. S. You, M. H. Chang, W. Yin, T. K. Ahn, S.-J. Lee, S.-J. Sung, D. H. Kim, S. H. Im, *Nano Energy* **2015**, *15*, 530.
[20] F. Giordano, A. Abate, J. P. Correa Baena, M. Saliba, T. Matsui, S. H. Im, S. M. Zakeeruddin, M. K. Nazeeruddin, A. Hagfeldt, M. Graetzel, *Nat. Commun.* **2016**, *7*, 10379.
[21] M. Saliba, T. Matsui, J.-Y. Seo, K. Domanski, J.-P. Correa-Baena, M. K. Nazeeruddin, S. M. Zakeeruddin, W. Tress, A. Abate, A. Hagfeldt, M. Grätzel, *Energy Environ. Sci.* **2016**, *9*, 1989.
[22] N. J. Jeon, J. H. Noh, W. S. Yang, Y. C. Kim, S. Ryu, J. Seo, S. I. Seok, *Nature* **2015**, *517*, 476.
[23] H. Si, Q. Liao, Z. Zhang, Y. Li, X. Yang, G. Zhang, Z. Kang, Y. Zhang, *Nano Energy* **2016**, *22*, 223.
[24] K. Wang, Y. Shi, B. Li, L. Zhao, W. Wang, X. Wang, X. Bai, S. Wang, C. Hao, T. Ma, *Adv. Mater.* **2016**, *28*, 1891.
[25] W. Ke, G. Fang, Q. Liu, L. Xiong, P. Qin, H. Tao, J. Wang, H. Lei, B. Li, J. Wan, G. Yang, Y. Yan, *J. Am. Chem. Soc.* **2015**, *137*, 6730.
[26] X. Liu, K.-W. Tsai, Z. Zhu, Y. Sun, C.-C. Chueh, A. K. Y. Jen, *Adv. Mater. Interfaces* **2016**, *3*, 1600122.
[27] J. P. Correa Baena, L. Steier, W. Tress, M. Saliba, S. Neutzner, T. Matsui, F. Giordano, J. Jacobsson, A. R. Srimath Kandada, S. M. Zakeeruddin, A. Petrozza, A. Abate, K. N. Mohammad, M. Grätzel, A. Hagfeldt, *Energy Environ. Sci.* **2015**, *8*, 2928.
[28] A. H. Ip, L. N. Quan, M. M. Adachi, J. J. McDowell, J. Xu, D. H. Kim, E. H. Sargent, *Appl. Phys. Lett.* **2015**, *106*, 143902.
[29] K. Wojciechowski, S. D. Stranks, A. Abate, G. Sadoughi, A. Sadhanala, N. Kopidakis, G. Rumbles, C.-Z. Li, R. H. Friend, A. K.-Y. Jen, *ACS Nano* **2014**, *8*, 12701.
[30] Y. Hou, C. O. R. Quiroz, S. Scheiner, W. Chen, T. Stubhan, A. Hirsch, M. Halik, C. J. Brabec, *Adv. Energy Mater.* **2015**, *5*, 1501056.
[31] C. Zhao, B. Chen, X. Qiao, L. Luan, K. Lu, B. Hu, *Adv. Energy Mater.* **2015**, *5*, 1500279.
[32] A. Fakharuddin, F. Di Giacomo, A. L. Palma, F. Matteocci, I. Ahmed, S. Razza, A. D'Epifanio, S. Licoccia, J. Ismail, A. Di Carlo, *ACS Nano* **2015**, *9*, 8420.
[33] S. Dharani, H. K. Mulmudi, N. Yantara, P. T. Thu Trang, N. G. Park, M. Graetzel, S. Mhaisalkar, N. Mathews, P. P. Boix, *Nanoscale* **2014**, *6*, 1675.
[34] D. Zhong, B. Cai, X. Wang, Z. Yang, Y. Xing, S. Miao, W.-H. Zhang, C. Li, *Nano Energy* **2015**, *11*, 409.
[35] D.-Y. Son, J.-H. Im, H.-S. Kim, N.-G. Park, *J. Phys. Chem. C* **2014**, *118*, 16567.
[36] K. Mahmood, B. S. Swain, A. Amassian, *Adv. Energy Mater.* **2015**, *5*, 1500568.
[37] G. Yang, H. Tao, P. Qin, W. Ke, G. Fang, *J. Mater. Chem. A* **2016**, *4*, 3970.
[38] J. Xing, W. Q. Fang, Z. Li, H. G. Yang, *Ind. Eng. Chem. Res.* **2012**, *51*, 4247.
[39] H. Song, K. H. Lee, H. Jeong, S. H. Um, G. S. Han, H. S. Jung, G. Y. Jung, *Nanoscale* **2013**, *5*, 1188.
[40] P. Qin, A. L. Domanski, A. K. Chandiran, R. Berger, H. J. Butt, M. I. Dar, T. Moehl, N. Tetreault, P. Gao, S. Ahmad, M. K. Nazeeruddin, M. Gratzel, *Nanoscale* **2014**, *6*, 1508.
[41] S. K. Pathak, A. Abate, P. Ruckdeschel, B. Roose, K. C. Gödel, Y. Vaynzof, A. Santhala, S.-I. Watanabe, D. J. Hollman, N. Noel, A. Sepe, U. Wiesner, R. Friend, H. J. Snaith, U. Steiner, *Adv. Funct. Mater.* **2014**, *24*, 6046.
[42] J. Wang, M. Qin, H. Tao, W. Ke, Z. Chen, J. Wan, P. Qin, L. Xiong, H. Lei, H. Yu, G. Fang, *Appl. Phys. Lett.* **2015**, *106*, 121104.
[43] D. H. Kim, G. S. Han, W. M. Seong, J. W. Lee, B. J. Kim, N. G. Park, K. S. Hong, S. Lee, H. S. Jung, *ChemSusChem* **2015**, *8*, 2392.
[44] M. Khan, W. Cao, *J. Mol. Catal. A: Chem.* **2013**, *376*, 71.
[45] H. Zhang, K. Tan, H. Zheng, Y. Gu, W. F. Zhang, *Mater. Chem. Phys.* **2011**, *125*, 156.
[46] H. Uchiyama, H. Ohgi, H. Imai, *Cryst. Growth Des.* **2006**, *6*, 2186.
[47] S. M. Kang, S. Jang, J. K. Lee, J. Yoon, D. E. Yoo, J. W. Lee, M. Choi, N. G. Park, *Small* **2016***12*, 2443.
[48] J. Dong, J. Shi, D. Li, Y. Luo, Q. Meng, *Appl. Phys. Lett.* **2015**, *107*, 073507.
[49] E. Guillén, F. J. Ramos, J. A. Anta, S. Ahmad, *J. Phys. Chem. C* **2014**, *118*, 22913.
[50] T. Oku, M. Kanayama, Y. Ono, T. Akiyama, Y. Kanamori, M. Murozono, *Jpn. J. Appl. Phys.* **2014**, *53*, 05FJ03.
[51] S. Jang, J. Yoon, K. Ha, M.-C. Kim, D. H. Kim, S. M. Kim, S. M. Kang, S. J. Park, H. S. Jung, M. Choi, *Nano Energy* **2016**, *22*, 499.
[52] W.-Q. Wu, F. Huang, D. Chen, Y.-B. Cheng, R. A. Caruso, *Adv. Funct. Mater.* **2015**, *25*, 3264.
[53] M. Park, J.-Y. Kim, H. J. Son, C.-H. Lee, S. S. Jang, M. J. Ko, *Nano Energy* **2016**, *26*, 208.
[54] W.-Q. Wu, F. Huang, D. Chen, Y.-B. Cheng, R. A. Caruso, *Adv. Energy Mater.* **2016**, *6*, 1502027.
[55] S. Ryu, J. H. Noh, N. J. Jeon, Y. Chan Kim, W. S. Yang, J. Seo, S. I. Seok, *Energy Environ. Sci.* **2014**, *7*, 2614.
[56] Q. Hu, J. Wu, C. Jiang, T. Liu, X. Que, R. Zhu, Q. Gong, *ACS Nano* **2014**, *8*, 10161.
[57] Y. Zhao, C. Liang, H. Zhang, D. Li, D. Tian, G. Li, X. Jing, W. Zhang, W. Xiao, Q. Liu, *Energy Environ. Sci.* **2015**, *8*, 1256.
[58] Y. Zhang, M. Liu, G. E. Eperon, T. C. Leijtens, D. McMeekin, M. Saliba, W. Zhang, M. de Bastiani, A. Petrozza, L. M. Herz, M. B. Johnston, H. Lin, H. J. Snaith, *Mater. Horiz.* **2015**, *2*, 315.
[59] S. H. Im, J.-H. Heo, H. J. Han, D. Kim, T. Ahn, *Energy Environ. Sci.* **2015**, *8*, 1602.
[60] Y. Zhao, C. Liang, H. Zhang, D. Li, D. Tian, G. Li, X. Jing, W. Zhang, W. Xiao, Q. Liu, F. Zhang, Z. He, *Energy Environ. Sci.* **2015**, *8*, 1256.
[61] E. L. Unger, E. T. Hoke, C. D. Bailie, W. H. Nguyen, A. R. Bowring, T. Heumüller, M. G. Christoforo, M. D. McGehee, *Energy Environ. Sci.* **2014**, *7*, 3690.
[62] K. Mahmood, B. S. Swain, A. Amassian, *Adv. Mater.* **2015**, *27*, 2859.
[63] J. Mai, T.-K. Lau, J. Li, S.-H. Peng, C.-S. Hsu, U. S. Jeng, J. Zeng, N. Zhao, X. Xiao, X. Lu, *Chem. Mater.* **2016**, *28*, 6186.

Received: May 26, 2016
Revised: September 8, 2016
Published online: November 7, 2016

 © 2016 Wiley-VCH Verlag GmbH & Co. KGaA, Weinheim